



Multimodality imaging reveals angiogenic evolution in vivo during calvarial bone defect healing

Yunke Ren¹ · Xinying Chu¹ · Janaka Senarathna^{2,3} · Akanksha Bhargava² · Warren L. Grayson^{1,5,6,8,9} · Arvind P. Pathak^{1,2,4,7,9}

Received: 19 July 2023 / Accepted: 27 October 2023 / Published online: 30 November 2023
© The Author(s), under exclusive licence to Springer Nature B.V. 2023

Abstract

The healing of calvarial bone defects is a pressing clinical problem that involves the dynamic interplay between angiogenesis and osteogenesis within the osteogenic niche. Although structural and functional vascular remodeling (i.e., angiogenic evolution) in the osteogenic niche is a crucial modulator of oxygenation, inflammatory and bone precursor cells, most clinical and pre-clinical investigations have been limited to characterizing structural changes in the vasculature and bone. Therefore, we developed a new multimodality imaging approach that for the first time enabled the longitudinal (i.e., over four weeks) and dynamic characterization of multiple in vivo functional parameters in the remodeled vasculature and its effects on de novo osteogenesis, in a preclinical calvarial defect model. We employed multi-wavelength intrinsic optical signal (IOS) imaging to assess microvascular remodeling, intravascular oxygenation (SO₂), and osteogenesis; laser speckle contrast (LSC) imaging to assess concomitant changes in blood flow and vascular maturity; and micro-computed tomography (μCT) to validate volumetric changes in calvarial bone. We found that angiogenic evolution was tightly coupled with calvarial bone regeneration and corresponded to distinct phases of bone healing, such as injury, hematoma formation, revascularization, and remodeling. The first three phases occurred during the initial two weeks of bone healing and were characterized by significant in vivo changes in vascular morphology, blood flow, oxygenation, and maturity. Overall, angiogenic evolution preceded osteogenesis, which only plateaued toward the end of bone healing (i.e., four weeks). Collectively, these data indicate the crucial role of angiogenic evolution in osteogenesis. We believe that such multimodality imaging approaches have the potential to inform the design of more efficacious tissue-engineering calvarial defect treatments.

Keywords Imaging · Angiogenesis · Osteogenesis · Calvarial bone defect · Preclinical

✉ Arvind P. Pathak
apathak2@jhmi.edu

¹ Department of Biomedical Engineering, The Johns Hopkins University School of Medicine, Baltimore, MD, USA

² Present Address: Russell H. Morgan Department of Radiology and Radiological Science, The Johns Hopkins University School of Medicine, 720 Rutland Ave, 217 Traylor Bldg, Baltimore, MD 21205, USA

³ Kavli Neuroscience Discovery Institute, The Johns Hopkins University School of Medicine, Baltimore, MD, USA

⁴ The Sidney Kimmel Comprehensive Cancer Center, The Johns Hopkins University School of Medicine, Baltimore, MD, USA

⁵ Department of Materials Science and Engineering, The Johns Hopkins University School of Medicine, Baltimore, MD, USA

⁶ Chemical and Biomolecular Engineering, Johns Hopkins University, Baltimore, MD, USA

⁷ Electrical Engineering, Johns Hopkins University, Baltimore, MD, USA

⁸ Translational Tissue Engineering Center, Johns Hopkins University, Baltimore, MD, USA

⁹ Institute for Nanobiotechnology, Johns Hopkins University, Baltimore, MD, USA

Introduction

The treatment of calvarial bone injuries has long posed a clinical challenge because of our limited understanding of the *in vivo* interplay between structural and functional vascular remodeling (i.e., “angiogenic evolution”) and osteogenesis. Calvarial bone healing induces dynamic changes in the “osteogenic niche” that regulate multiple signaling pathways, activities of the bone-forming cells, the *de novo* growth of blood vessels (i.e., angiogenesis) and concomitant functional changes in perfusion and oxygenation [1, 2]. While many studies have characterized the direct contribution of osteogenic cells to bone formation [3, 4], *in vivo* assessments of angiogenic evolution within the osteogenic niche during bone healing remain limited [5]. Recent advances in *in vivo* imaging in conjunction with novel preclinical bone defect models have enabled the interrogation of structural vascular changes during angiogenic evolution with high spatial and temporal resolution, contrast-to-noise ratio (CNR), spatial coverage, and longitudinal tracking capabilities [1]. However, functional aspects of angiogenic evolution have not been elucidated at microvascular spatial scales over the calvarial bone healing cycle. This is largely due to a lack of imaging approaches that integrate complementary contrast mechanisms capable of simultaneously assessing *in vivo* changes in perfusion and intravascular oxygenation [1, 6]. While recent research has revealed increased blood flow and oxygenation in specific vascular phenotypes (e.g., “type H” vessels) during calvarial bone healing [7], it remains unclear how these change dynamically within the osteogenic niche during the different phases of bone healing.

To address these questions, we developed a multimodality *in vivo* imaging method for characterizing angiogenic evolution in a calvarial defect model over four weeks of bone healing. This approach combined intrinsic optical signal (IOS) imaging, laser speckle contrast (LSC) imaging and micro-computed tomography (μ CT) at microvascular spatial resolution with a novel image-processing pipeline that enabled “image-based vascular phenotyping” during angiogenic evolution. With this approach, we successfully quantified *in vivo* changes in blood vessel structure (i.e., vascular remodeling) and function (i.e., perfusion and oxygenation) and their impact on osteogenesis. Furthermore, we successfully integrated *in vivo* and *ex vivo* imaging data to visualize the spatiotemporal correlations between angiogenesis and osteogenesis over the calvarial bone healing cycle.

Methods

Animal surgery

All animal experiments were conducted in accordance with an approved Johns Hopkins University Animal Care and Use Committee (JHU ACUC) protocol. The Johns Hopkins University animal facility is accredited by the American Association for the Accreditation of Laboratory Animal Care and meets the National Institutes of Health (NIH) standards as set forth in the “Guide for the Care and Use of Laboratory Animals.” Ten 10-week-old male C57BL/6 mice (Jackson Laboratories, Bar Harbor, ME) were anesthetized with intraperitoneal administration of 0.15 ml of a mixture of ketamine (80 mg/kg) and xylazine (8 mg/kg). Next, 0.5 ml of dexamethasone (2 mg/ml) and buprenorphine (1 mg/ml) were administered subcutaneously to reduce inflammation and pain. All surgical devices were sterilized. After sedation level was confirmed with a paw-pinch test, the surgical region was shaved and sterilized by swabbing with alcohol and betadine. The animal’s eyes were protected with ophthalmic lubrication ointment after which it was then placed in a stereotaxic frame. The skin above the calvarium was removed with a surgical scissor and any remaining tissue on the skull removed with 3% hydrogen peroxide solution. The skull was then flushed with cool saline and dried with cotton-tipped applicators. The center of the defect was identified at 2 mm above the lambdoid suture and 2 mm to the right of the sagittal suture for each mouse. A 2 mm circular region was then marked around this center, and a dental drill (Wave Dental Carbide Handpiece Burs, Round, HP1/4) used to carefully drill within the marked circle without damaging the underlying brain. While drilling, cold saline was used to irrigate the surgical field to remove any bone shavings and to prevent heating the brain. The drilled piece of calvarium was then carefully removed while leaving the dura intact. Cold saline was used to flush the defect and reduce micro-bleeds, if any. A 3 mm diameter coverslip was then placed on top of the defect and glued to the skull using gel superglue. Finally, dental cement was applied around the edge of the optical window to secure it and cover any exposed skull.

In Vivo imaging

From the day of the surgery (D0), cranial window-bearing animals underwent *in vivo* imaging every other day for four weeks using a customized multimodality imaging system (Fig. 1a). During imaging, each mouse was anesthetized using 1.5% isoflurane (Iso Flo, Cat. No.

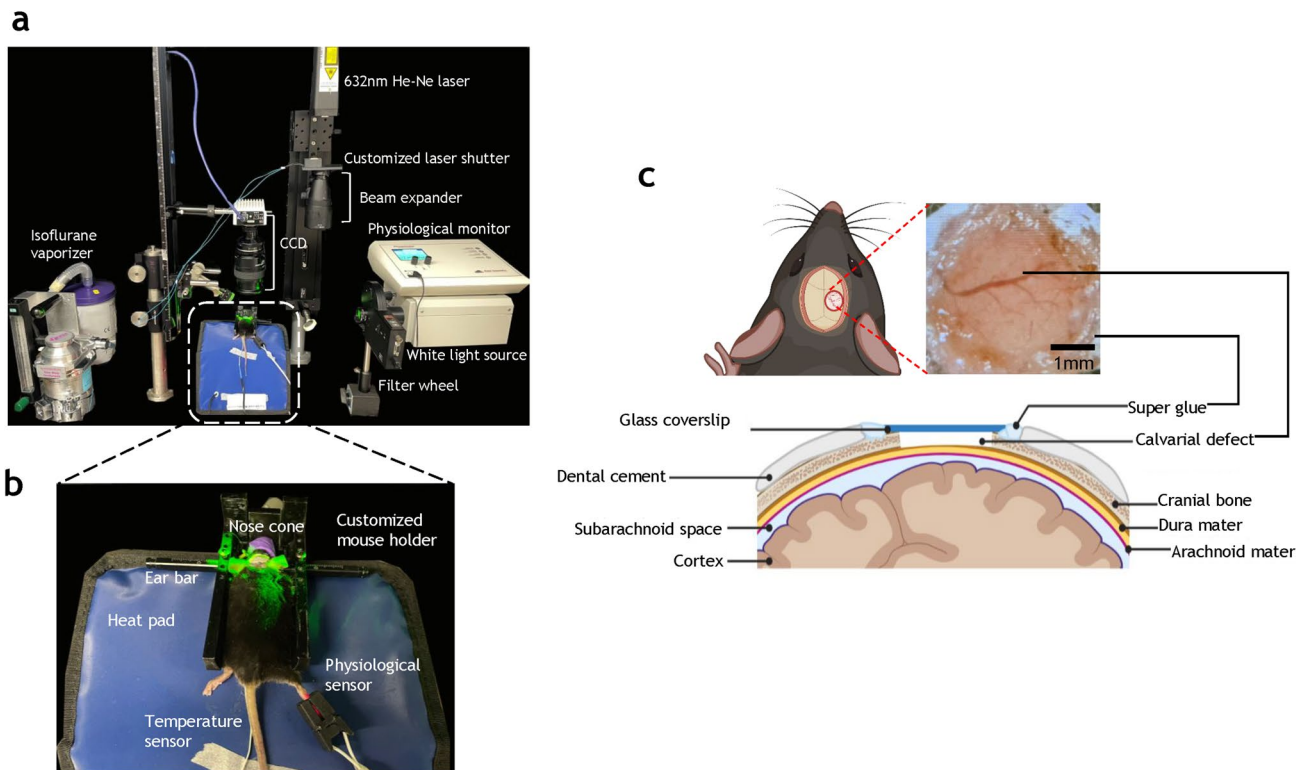


Fig. 1 Multimodality imaging system for characterizing angiogenic evolution in vivo in a preclinical calvarial defect healing model. **a** Photograph of the multimodal in vivo imaging system. The mouse was continuously anesthetized in a customized mouse holder connected to an isoflurane vaporizer for controlled anesthesia. The illumination source for in vivo Intrinsic Optical Signal (IOS) imaging was derived from a white light source and a filter wheel equipped with 570 ± 2 nm and 600 ± 8 nm bandpass filters. The illumination source for in vivo Laser Speckle Contrast (LSC) imaging was a 632 nm He–Ne laser coupled with a beam expander to illuminate the 3 mm cranial window field of view (FoV). The scattered light passes through a 496 nm long-pass filter and a $2\times$ focusing lens before being

detected by a CCD image sensor. The acquired images were saved to an external hard drive for further analysis. In addition, the mouse's vital parameters (i.e., heart rate, respiration, systemic oxygen saturation or SpO_2 , and body temperature) were tracked using a physiological monitor during all in vivo imaging. **b** Photograph illustrating the customized mouse holder, physiological monitoring sensors and heating pad employed during in vivo imaging. **c** Schematic illustrating a 2 mm full-thickness calvarial defect created on the murine parietal bone. A 3 mm cover slip was glued on the calvarial bone to protect the defect while permitting longitudinal in vivo imaging of angiogenesis and osteogenesis

06-8550-2/R1) in 1.5 L/min air delivered via a Vapomatic Model 2 vaporizer (AM Bickford, Inc., NY). The animal's head was fixed in a customized frame (Fig. 1b) and anesthesia continuously administered. A physiological monitoring system (PhysioSuite[®], Kent Scientific Corporation, CT) was used to monitor and maintain the physiological status of the mice, including heart rate, systemic oxygen saturation (SpO_2), respiration rate, and body temperature. Via the cranial window (Fig. 1c), we conducted in vivo IOS imaging at a high spatial ($5 \mu\text{m}$) and temporal resolution (200 ms). We used a white light source (NI-150, Nikon Instruments, Inc., NY) coupled with 530 ± 2 nm, 570 ± 2 nm, and 600 ± 8 nm band-pass filters (FB530-10, FB570-10, and FB600-40, Thorlabs, NJ) mounted on a filter wheel (FW102C, Thorlabs, NJ). IOS imaging utilized the wavelength-dependent absorption of hemoglobin

to differentiate blood vessels from the surrounding tissue, as hemoglobin-rich blood vessels absorb light and appear darker [8]. We also performed in vivo LSC imaging to visualize dynamic changes in blood flow in real-time. LSC imaging was possible because moving red blood cells (RBCs) created interference patterns under the coherent light illumination [9] provided by a 632.8 nm He–Ne laser (HNLS008R, Thorlabs, NJ) in our setup. Light reflected from the cranial window during IOS or LSC imaging was collected through a lens set (AF Micro Nikon 60 mm 1:2.8D, Nikon Instruments Inc., NY) and directed onto a charge coupled device (CCD) image sensor (CCD camera, Infinity 3, Lumenera, Ontario). The CCD was connected to a PC, which stored images via a custom MATLAB[®] program (MathWorks Inc, MA).

Carbogen gas challenge

To evaluate the maturity of the vasculature, a carbogen gas inhalation challenge was performed every other day starting on D2 post-surgery. During each carbogen gas challenge experiment, the mouse was anesthetized, and its physiology monitored using the same system as described previously, and images were acquired during breathing of the 1.5 L/min air for 5 min as a baseline condition before carbogen inhalation, during which room air was substituted with carbogen gas (95% O₂ and 5% CO₂) for 5 min, followed by 7 min of baseline conditions (i.e., breathing air). Images were continuously acquired during these 17 min. A customized MATLAB script controlled the acquisition of 530 nm, 600 nm, and LSC images every 30 s to compute changes in intravascular oxygen saturation (SO₂) and blood flow, respectively.

Vascular labeling with VasuViz for ex vivo μ CT imaging

At the end of weeks 1, 2, and 3 (i.e., on D8, D14, and D22), one animal was perfused using our VasuViz protocol [10] for ex vivo μ CT imaging of bone and blood vessel architecture. Using the same protocol, all remaining mice were perfused at the end of week 4. Briefly, 0.1 mL of BriteVu Enhancer[®] (Scarlet Imaging, UT) was added to 25 mL of distilled water at 40–45 °C and stirred for one minute on a hot plate. Next, 7 g of BriteVu[®] CT contrast agent (BVu, Scarlet Imaging, UT) was added to the solution and stirred until the temperature reached 60–70 °C (~10 min). This BVu solution was then maintained in a water bath until its temperature reached ~40–50 °C prior to perfusion. For transcatheter perfusion, the animal was anesthetized using ketamine/xylazine at 0.1 mL/10 g body weight. Then 10–15 mL of heparinized phosphate-buffered saline (PBS) and 10–15 mL of 10% buffered formalin were injected transcatheterially at 0.1 mL/s. Following that, the animal was perfused with 15–20 mL of the warm BVu (~40–50 °C) at 0.03 mL/s. After the perfusion, the head was excised and fixed overnight in cold 10% buffered formalin in the dark at 4 °C.

Micro-CT (μ CT) imaging

To prepare the fixed samples for μ CT imaging, we first removed the soft tissue surrounding the skull. Immediately before imaging, 10 ml of 4% (40 mg/mL) agarose solution (A9539 Sigma-Aldrich) was prepared for embedding the skull in a 15 mL Eppendorf tube that was cut in half and sealed with parafilm. μ CT images were then acquired on a Skyscan 1275 scanner (Bruker, MA) with the following acquisition parameters: 0.5 mm aluminum filter, 15 μ m pixel

size, 55 kV, 145 μ A, 335 ms exposure time, 0.5 rotation step, 5 averages, and 180° scan. 3D reconstruction was performed using the NRecon software (v.1.7.0.4, Bruker, MA).

Image processing

IOS and LSC images were processed using ImageJ [11] and MATLAB. First, all images were co-registered to the DO images for each mouse using the “affine registration” feature of the ImageJ plugin TurboReg [12]. To extract vascular morphological parameters from the registered IOS images, we first segmented the blood vessels (i.e., background = 0 and blood vessel = 1) manually using a digital tablet and stylus. The binary representations of blood vessels were processed in ImageJ to derive the centerline for each via the “skeletonization” function; the tagged skeleton (i.e., branch points) via the “analyze skeleton” function; and the Euclidean distance map via the “Distance map” function. We then imported these images into a customized MATLAB script to derive multiple morphological parameters including blood vessel length, volume, density, and tortuosity.

In addition, multi-wavelength IOS images were used to compute the intravascular SO₂. To do this, we utilized our recently developed method [13] to compute the vasculature-specific optical path-length, which was then combined with the absorption of hemoglobin derived from the 570 nm and 600 nm IOS images to calculate the concentration of oxy-hemoglobin C_{HbO_2} , and deoxyhemoglobin C_{HbR} . From that, the intravascular SO₂ was calculated according to:

$$SO_2(\%) = \frac{C_{HbO_2}}{C_{HbO_2} + C_{HbR}} \times 100 \quad (1)$$

To compute the relative blood flow from LSC images, we first calculated the degree of blurring or the speckle contrast from an LSC image stack consisting of 200 images using the following equation [9]:

$$K(x, y) = \frac{\sigma_N}{\mu_N} \quad (2)$$

where σ_N and μ_N are the standard deviation and mean pixel intensities computed from the time series of 200 images. Since the local speckle contrast K is inversely proportional to the blood flow, a heat map of the inverse of K was used to visualize the relative blood flow.

To quantify vascular maturity, we calculated the increase in blood flow in response to the carbogen gas challenge using the following equation:

$$\text{Vascular maturity}(\%) = \frac{BF_c - BF_b}{BF_b} \times 100 \quad (3)$$

where BF_c is the blood flow during carbogen challenge, and BF_b is the blood flow at baseline. The assumption underlying these calculations is that vasodilation in response to carbogen gas inhalation is directly proportional to its smooth muscle coverage, which is representative of the maturity of that vascular segment [14]. We implemented K-means clustering by using the vascular maturity calculated for each vascular segment as the input, which resulted in two statistically well-separated vessel classes. We defined the class with higher vascular maturity as being “mature vessels,” and the other as being “developing vessels.”

The spatial distribution of each of the structural and functional vascular variables was visualized using a bespoke radial plot. Briefly, the defect area was divided into twelve sectors and six concentric rings to create a radial grid. For each defect, the mean and standard deviation of each vascular variable was computed within each radial grid element. The mean value was then computed and mapped across all the animals.

To quantify bone growth from 2D IOS images, we first segmented the bone using Ilastik (v 1.3) [15], an interactive machine-learning based segmentation tool kit. Since bone is a highly reflective tissue, in IOS images it appeared bright (relative to the vasculature) with distinct edges. These features enabled us to “train” Ilastik to distinguish between bone and background pixels. The resulting bone “masks” were then used to calculate the fraction of bone growth within the defect.

Segmentation of bone and VascuViz-perfused vasculature from the 3D μ CT images was also conducted using Ilastik. Next, the 3D visualization and quantification of the degree of bone growth and vascularization were quantified using Amira[®] Software (Thermo Scientific[™], MA). Reconstructed μ CT images of the calvarium were imported into Amira[®], and the “volume rendering” function used to visualize the skull and blood vessels in 3D. To quantify osteogenesis within the defect, the defect region was cropped and the bone within selected using the “threshold” tool in the segmentation editor. The volume of the segmented bone was then be computed using the “material statistics” tool in Amira[®].

Statistical analysis

Bone healing experiments were performed in 10 mice. One mouse was sacrificed on days (D) 7 and 14, and two mice sacrificed on D21 for μ CT analyses of bone growth and vascular structure in 3D. The remaining mice ($n=6$) were sacrificed at the endpoint of the study (i.e., D28), and their in vivo data used for statistical analyses of the structural and functional blood vessel parameters. We first performed repeated measures ANOVA to assess whether there were significant differences in measurements across time points.

If the ANOVA indicated a significant difference, we used Bonferroni-corrected t-tests to determine which specific time points differed from each other. To compare blood flow and radii of the developing and mature vessels at each timepoint, we used the paired t-test. $P < 0.05$ was considered to be significant for all the employed tests.

Results

In vivo IOS imaging revealed robust vascular remodeling and changes in bone morphology during the calvarial defect healing cycle

We acquired IOS images from ten animals with 2 mm calvarial defects over four weeks of the bone healing cycle (Fig. 2a). Due to the light absorption by hemoglobin, blood vessels appeared dark in the IOS images [8]. Conversely, since bone scatters light, it appeared bright within the field of view (FoV). While the vasculature was clearly distinguishable on the day of surgery (Fig. 2a, D0) and two days after defect creation (Fig. 2a, D2), a hematoma occupied the field of view at D4, and gradually resolved over the next four days (Fig. 2a, D4–D8). Angiogenic vessels appeared within the defect on D6 and extended toward the edge of the defect by D8 (Fig. 2a, c). The diameter and density of these angiogenic vessels continued to increase from D8 to D12, and plateaued by the end of the second week (Fig. 2a, c). During this time, continual osteogenesis from D0 through D20 was clearly visible as brighter regions within the FoV (Fig. 2a). This bone growth was more evident on the digitally segmented images shown in Fig. 2b.

Blood vessel length (Fig. 2d), volume (Fig. 2e), and density (Fig. 2f) exhibited similar trends during bone healing with the largest changes in each parameter occurring during the first two weeks. The total blood vessel length decreased by 100% from D2 to D4, and increased by over 400% over the next four days ($p < 0.05$); the total blood volume also decreased by 100% from D2 to D4, and increased by 500% from $0.4 \mu\text{m}^3$ to $2 \mu\text{m}^3$ from D4 to D14 ($p=0.004$); the blood vessel density decreased by $\sim 150\%$ during the first two days, and increased by $\sim 700\%$ over the next eight days ($p=0.002$). The robust increase in these parameters was followed by a plateau toward the end of four weeks. Relative to angiogenic changes, osteogenic changes were more gradual, but exhibited similar trends (Fig. 2g). There was a significant ($p < 0.05$) increase in bone regrowth during the first two weeks of healing, with $\sim 40\%$ increase in bone volume by D14. The bone volume increased by an additional 10% over the next two weeks and covered 50% of the defect by the end of the fourth week.

We also stratified the vasculature by its tortuosity, length, and diameter to characterize changes during the four weeks

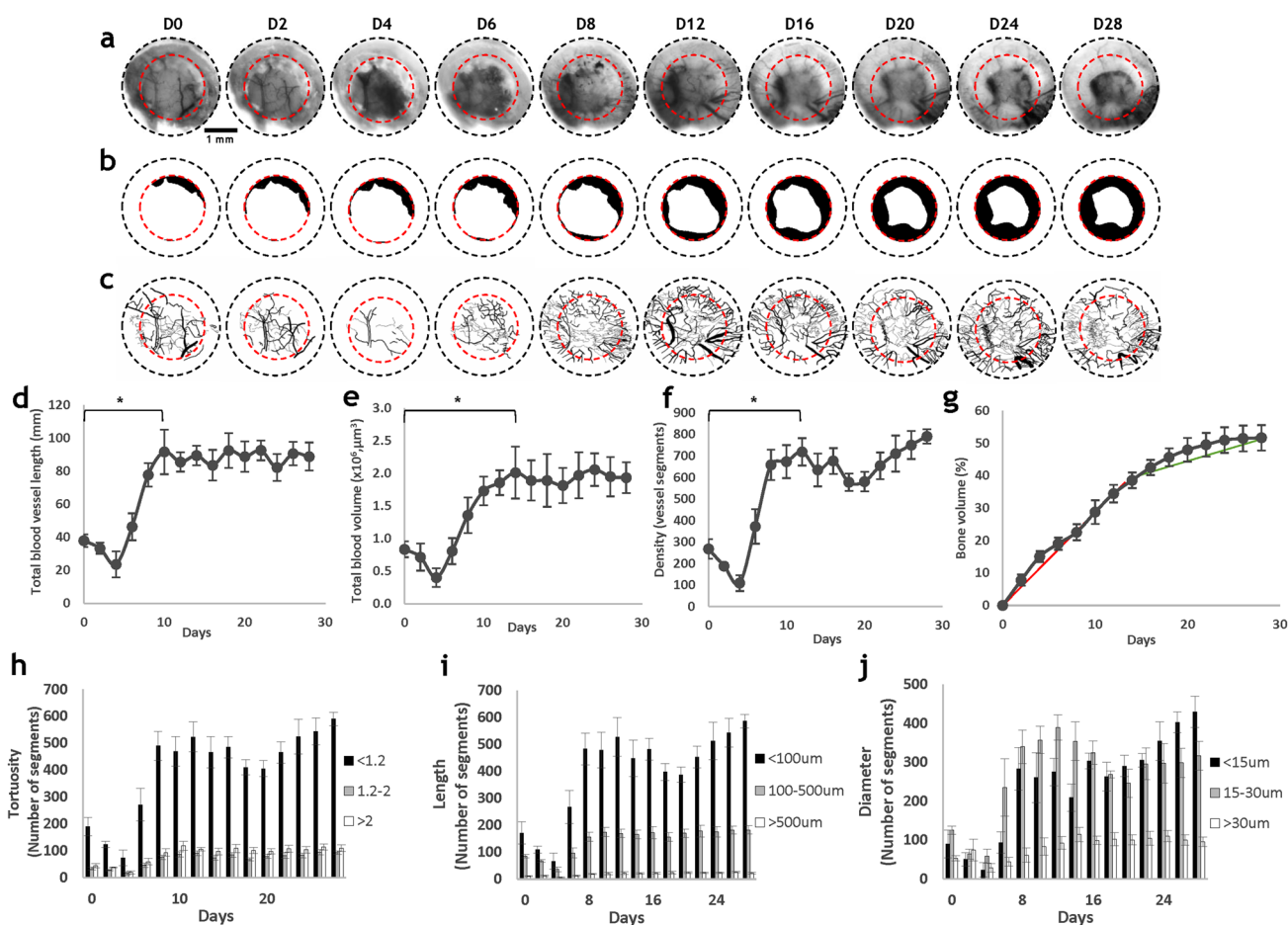


Fig. 2 In vivo IOS imaging revealed robust changes in vascular and bone morphology during the calvarial defect healing cycle. **a** IOS images showing the blood vessel and bone morphology within a calvarial defect. The black dashed circles represent the 3 mm FoV provided by the glass coverslip, and the red dashed circles represent the 2 mm defect. **b** Images of segmented bone illustrate the robust osteogenesis that occurred during 4 weeks of defect healing. **c** Images of segmented blood vessels showed robust angiogenesis concurrently

occurred. **d** Total blood vessel length; **e** total blood volume; and **f** blood vessel density increased during the first two weeks, and diminished during the final two weeks. **g** Bone volume fraction increased during the first two weeks, and plateaued during the final two weeks. The vasculature within the osteogenic niche was characterized by: **h** low tortuosity (<1.2); **i** small length (<100 μm); and **j** small diameter (<30 μm)

of calvarial bone healing (Fig. 2h–j). We found that the number of vessels with low tortuosity (<1.2) exhibited the most significant increase relative to baseline (D0 post-surgery) ($p=0.001$) in the vascular network, while the number of vessels with larger tortuosity (>1.2) did not change significantly during defect healing. Similarly, the number of blood vessels with small segment lengths (<100 μm) increased by more than ~500%, ($p=0.001$) during defect healing, and the number of medium length vessels (100–500 μm) increased by less than 100%. In contrast, the number of vessel segments of length >500 μm accounted for less than 5% of total number of vessel segments and did not change appreciably over four weeks. In terms of diameter, the number of small (<15 μm) and medium (15–30 μm) sized blood vessels significantly increased relative to the baseline during angiogenesis ($p=0.005$ and $p=0.003$, respectively), with both

exhibiting an increase of over 700% from D4 to D8. Interestingly, the number of small-sized blood vessels decreased from D8 to D14, while the number of medium sized vessels increased. This trend reversed from D20 to D28, with an increased number of small blood vessels and a plateau for the medium sized vessels. Finally, blood vessels with diameters exceeding 30 μm did not show as robust a change as the other two groups of vessels.

Measurements of osteogenesis from 2D in vivo imaging correlated strongly with those from 3D ex vivo μCT imaging

We correlated weekly measurements of bone area within the defect derived from 2D in vivo IOS images with 3D bone volume measurements (i.e., an index of osteogenesis) from

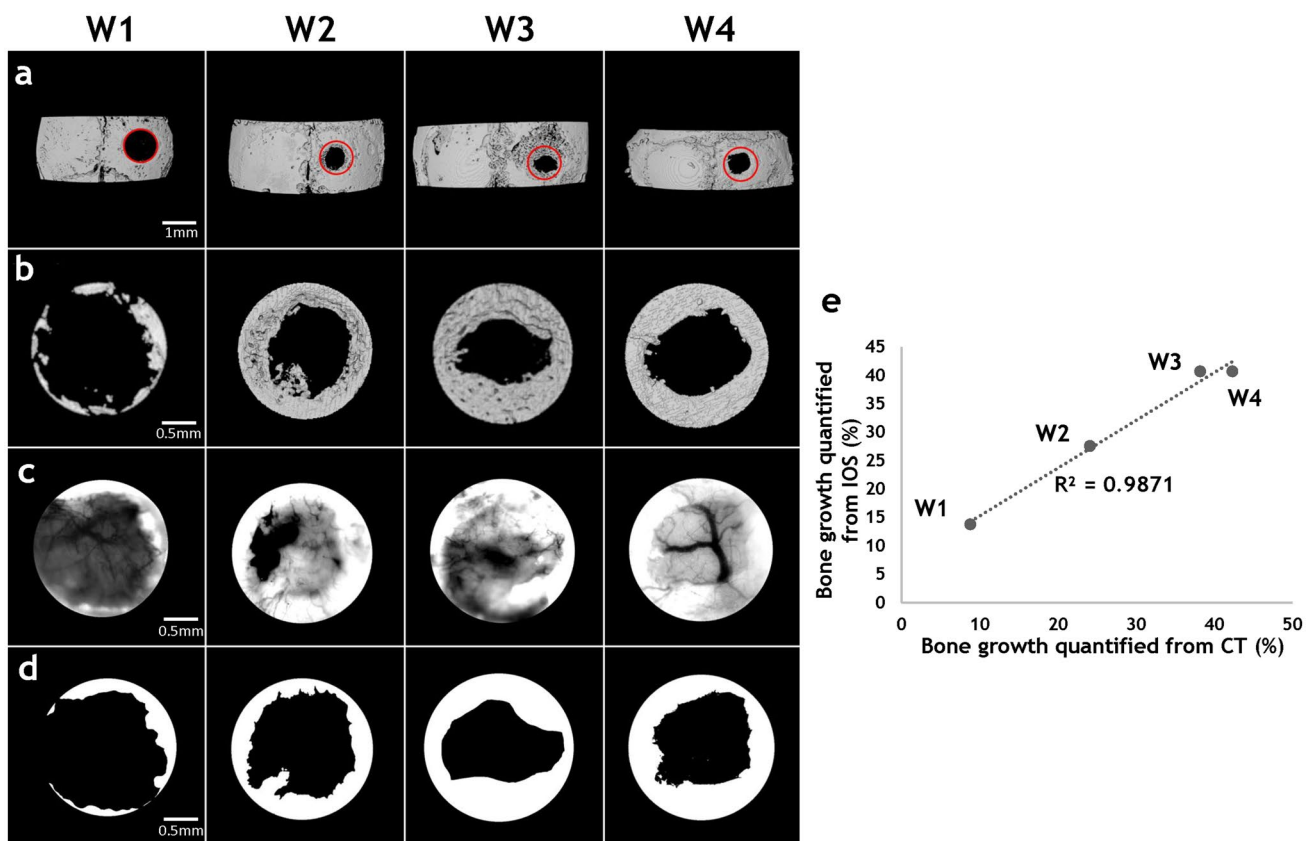


Fig. 3 Measurements of osteogenesis from 2D in vivo imaging strongly correlated with those from 3D ex vivo CT imaging. **a** μ CT images of the murine calvarium from animals euthanized at week 1, 2, 3, and 4 after defect creation. Red circles indicated the defect. **b** Images of the segmented bone volume from the red circled regions

in **(a)**. **c** IOS images of the same FoVs as in **(b)**, in which the highly scattering bone is clearly visible. **d** Images of the bone segmented from the 2D IOS images in **(c)**. **e** Scatter plot of fractional bone volume computed from 3D μ CT vs. that computed from 2D IOS images illustrates the strong correlation ($R^2 = 0.9871$) between them

ex vivo μ CT images. The measurement regions were identified on the μ CT images of the skull based on the location of the defect surgery on D0 (Fig. 3a), and the maximum intensity projections (MIP) of bone volumes within the defects (Fig. 3b) generated. Measurements of bone area (Fig. 3d) made from from IOS images (Fig. 3c) were then correlated with MIP of bone volume from the μ CT images of the same defects for the same time points (Fig. 3b). It was observed that the bone growth profile within the defect regions was similar across all time points using these two methods (Fig. 3b, d). We also correlated bone growth quantified from these two methods (Fig. 3e). Overall, IOS-derived measurements of bone area were strongly correlated ($R^2 = 0.9871$) with the μ CT-derived measurements of bone volume, indicating that osteogenic changes could be accurately tracked with in vivo IOS imaging.

LSC imaging revealed that angiogenic evolution within the osteogenic niche is characterized by in vivo changes in blood flow

On the day of surgery, the blood flow within the defect (Fig. 4, white dashed circle) was likely low because of possible blood vessel rupture during defect creation. From D0 to D2, blood flow increased by $\sim 100\%$. However, the blood flow on D4 was attenuated due to a hematoma (observable in the IOS channel, Fig. 2a), and inflammation was clearly visible on D6 in terms of a 60% elevation in blood flow relative to D4. When the hematoma resolved by D8, the blood flow within the defect returned to D2 levels and small angiogenic vessels around the defect edge started to be perfused. These angiogenic vessels continued exhibit perfusion

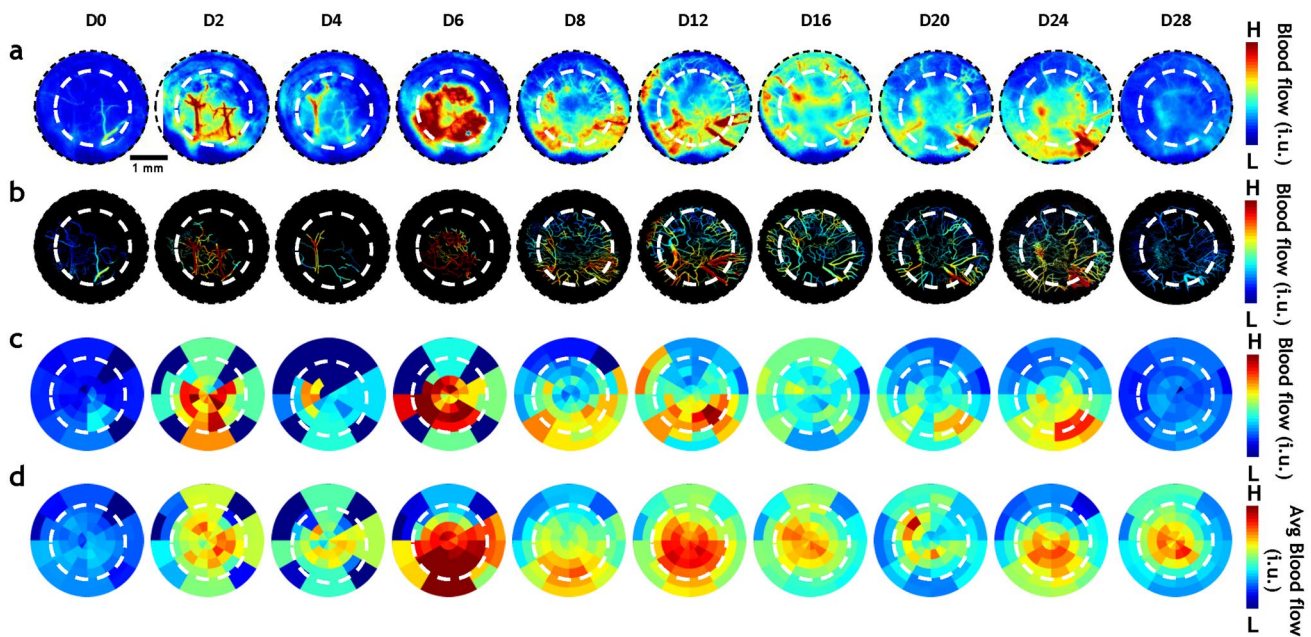


Fig. 4 In vivo LSC imaging revealed that angiogenic evolution within the osteogenic niche includes intricate blood flow changes. **a** In vivo blood flow changes within the calvarial defect (white dashed circle) of a representative animal. A robust increase in blood flow was observed during the first two weeks (D2–D16) of healing, followed by a decrease toward the end of the fourth week (D28). **b** The vascu-

lature corresponding to the images in **(a)** was segmented to highlight intravascular blood flow changes. **c** Radial plots for the same animal illustrate the spatio-temporal evolution of the mean blood flow within the calvarial defect over four weeks. **d** Radial plots of the mean blood flow changes computed for the entire cohort of animals ($n=6$)

into the second week of defect healing. After that, during the third week of defect healing, the increase in blood flow began to plateau, and by D28 returned to the baseline level observed at D0.

To visualize in vivo blood flow changes during angiogenic evolution (Fig. 4a), we first mapped blood flow onto the segmented vasculature for each time point (Fig. 4b). We then visualized the blood flow at each time point using radial plots as shown in Fig. 4c for a representative animal. The radial plots provide a universal space for mapping in vivo blood flow irrespective of the underlying vascular remodeling, and permit the visualization of blood flow changes during osteogenesis across all animals ($n=6$). The mean (Fig. 4d) blood flow maps indicated that there in vivo perfusion was elevated within the defect and attenuated outside it during the first week of bone healing. This was accompanied by an attenuation of blood flow within the defect from D6 to D8, followed by a return to elevated blood flow by D12, after which it plateaued.

Multi-wavelength IOS imaging revealed intravascular SO_2 changes accompanied angiogenic evolution within the osteogenic niche

Intravascular SO_2 was mapped during four weeks of calvarial bone healing by employing the changes in hemoglobin

concentration detected with multi-wavelength IOS imaging (Fig. 5a). During the first week of bone healing, the distribution of SO_2 was very heterogeneous, with the outside of the defect exhibiting low SO_2 because of poor vascularization (Fig. 5a D2–D6). From D6 when the hematoma began to resolve and angiogenic vessels formed, there was a 30% increase in SO_2 around the edge of the calvarial defect, or the active bone-growing regions. Toward the end of four weeks of bone healing when osteogenesis had plateaued, the SO_2 distribution within the defect became more homogenous. As before, we visualized the spatiotemporal changes in SO_2 during osteogenesis and angiogenesis at the individual (Fig. 5b) and group (Fig. 5c) levels using our radial plot approach.

Angiogenic vessels could be phenotyped in vivo based on their response to a carbogen gas challenge

We characterized the maturity of angiogenic vessels in vivo based on their ability to respond to carbogen gas. The segmented vasculature within the defect was overlaid with the blood flow change (ΔBF) in response to carbogen gas inhalation (Fig. 6a), and also mapped as a radial plot (Fig. 6b). It can be observed that at D2, most of the vessels within the FoV appeared to be responsive (i.e., mature) since they were primarily the preexisting dural vessels. The hematoma

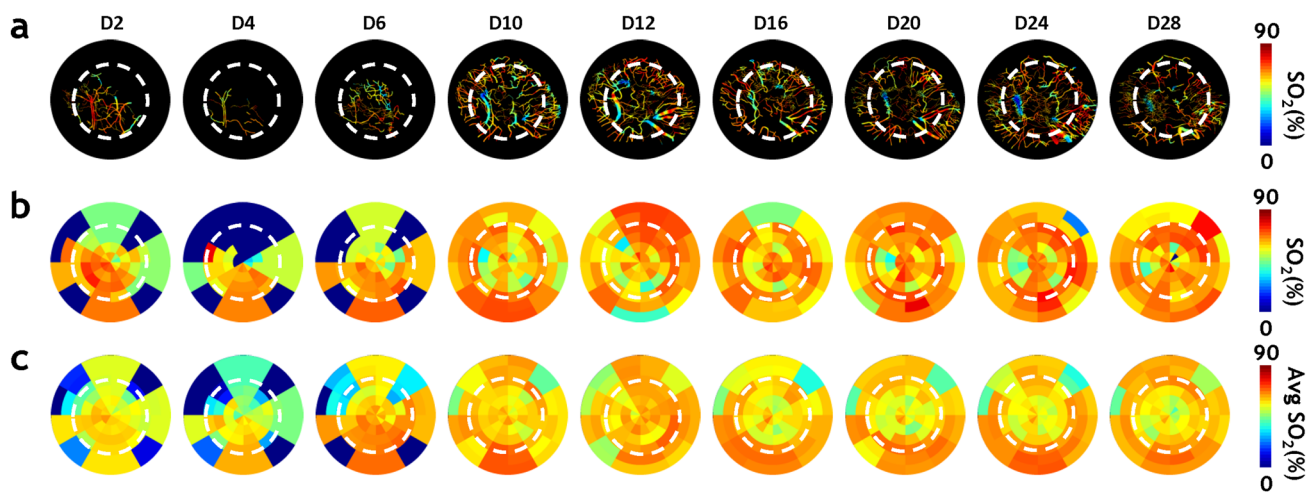


Fig. 5 In vivo multi-wavelength IOS imaging revealed that intravascular SO_2 changes accompany angiogenic evolution within the osteogenic niche. **a** Intravascular SO_2 computed from multi-wavelengths IOS images showed that angiogenic vessels near the defect edge (white dashed circle) exhibited elevated SO_2 during the 2nd week of healing compared to the rest of the vasculature within the FoV. **b** Radial plots for the same animal illustrate the spatio-temporal evolution

of the mean SO_2 within the calvarial defect over four weeks.. It was observed that SO_2 was inhomogenous during the first week (D2–D6) of healing, increased near the defect edge during the next 2–3 weeks (D10–D20) of healing, and became more homogenous throughout the defect toward the end of healing (D28). **c** Radial plots of the mean SO_2 changes computed for the entire cohort of animals ($n=6$)

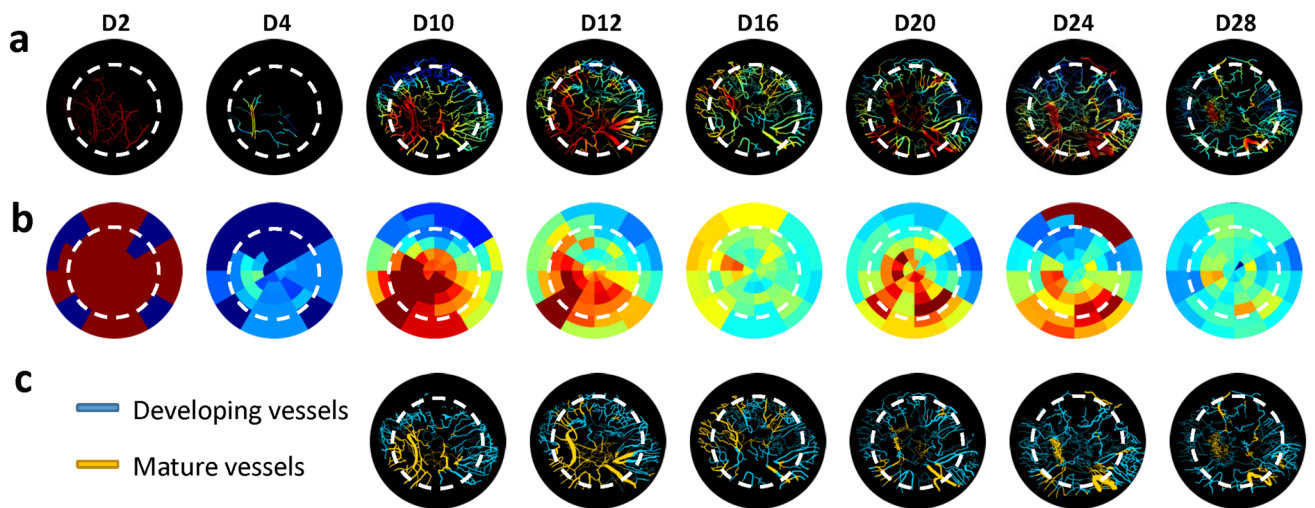


Fig. 6 Angiogenic vessels could be phenotyped based on their blood flow response to a carbogen gas challenge. **a** Vascular maturity computed from carbogen gas induced blood flow changes showed that the vascular bed exhibited heterogenous and continuously changing maturity levels during the 4-week healing cycle. **b** Radial plots for the same animal illustrate the spatio-temporal changes in vascular maturity

within the calvarial defect over four weeks. **c** K-means clustering helped classify the vascular bed within the defect into “developing” and “mature” vessels. More mature vessels were observed during robust bone healing phases (D12 and D16) than during the second week of healing (D20–D28)

in the defect at D4 obscured the ΔBF map. At D10 when angiogenic vessels appeared within the defect, the peripheral vessels exhibited the smallest ΔBF in response to carbogen, indicating that they were newly formed vessels that had not yet matured. As angiogenesis continued over the next few weeks of defect healing, the maturity of the vessels within the field of view also evolved (Fig. 6b). Starting at D10,

angiogenic vessels in the FoV could be spatially classified into two vascular phenotypes, i.e., “developing” or “mature” vessels (Fig. 6c) based on the magnitude of ΔBF during the carbogen challenge. Most angiogenic vessels around the defect edge were developing vessels, while those toward the defect center were mature vessels. Some angiogenic vessels on the defect edge evolved into mature vessels by D16.

Additionally, new angiogenic vessels continued to proliferate around the defect after D16, which resulted in more vessels of the developing vascular phenotype within the FoV.

To further characterize these vascular phenotypes within the defect, we also assessed their blood flow and average radii (Suppl Fig. 1a–b). We found that the distributions of blood flow and radii exhibited a rightward shift for the mature vessels compared to developing vessels. This difference in radii and blood flow was significant ($p < 0.05$) between developing and mature blood vessels within the defect. Collectively, these data indicate that mature vessels were characterized by larger radii and elevated perfusion

relative to developing blood vessels over the entire four week defect healing (Suppl Fig. 1c–d).

Angiogenic evolution correlated with the phases of the calvarial bone healing cycle

We plotted changes in the mean structural (i.e., total blood vessel length) and functional (i.e., blood flow and SO_2) vascular parameters during the four week defect healing cycle for all mice in the experimental cohort (Fig. 7a). Based on these plots, we successfully correlated angiogenic evolution during distinct phases of calvarial bone healing (Fig. 7b).

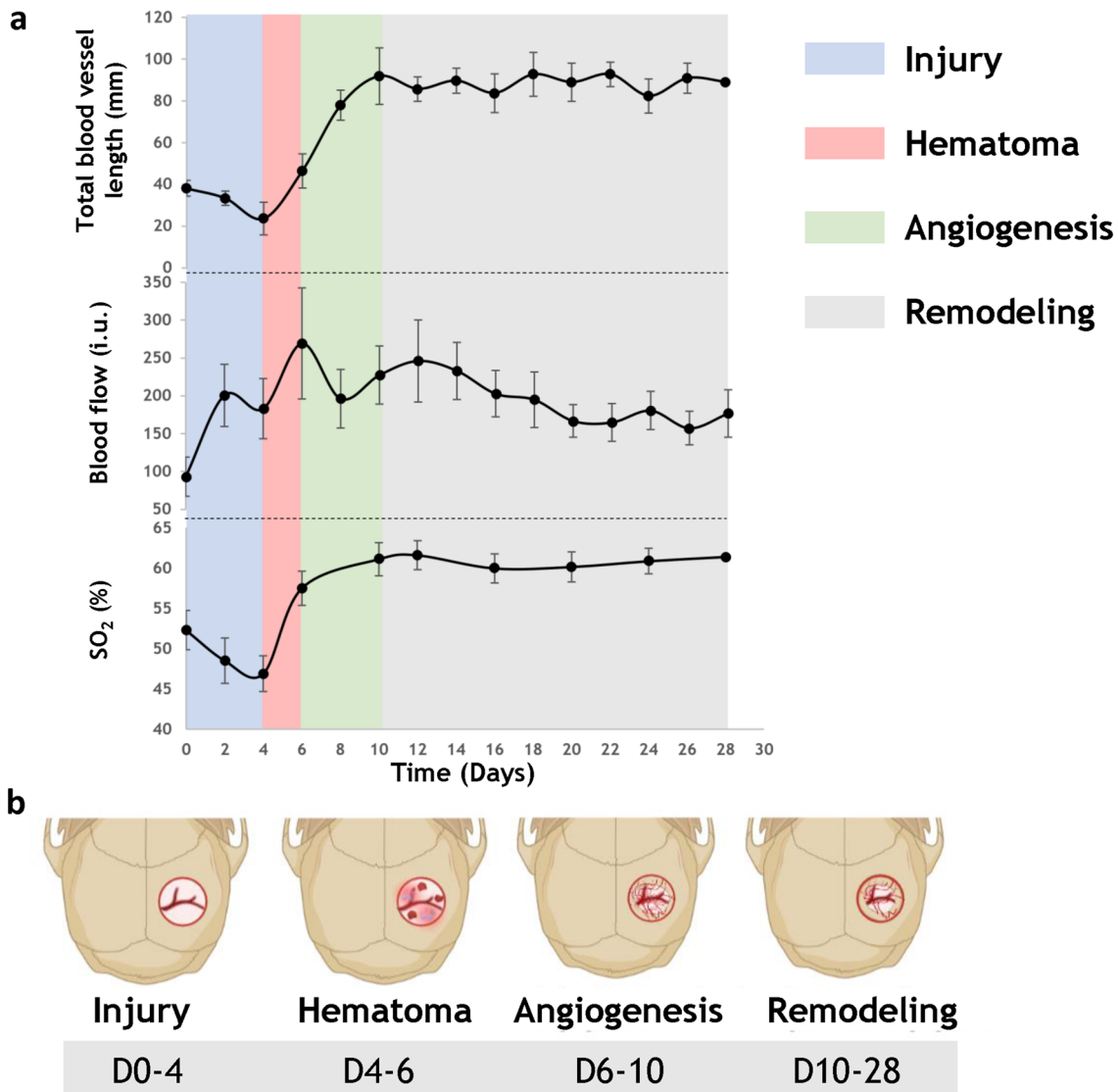


Fig. 7 Structural and functional vascular data revealed a correlation between angiogenic evolution and phases of the calvarial bone healing cycle in vivo. **a** Multimodality in vivo imaging permitted us to classify angiogenic evolution into distinct phases during four weeks of osteogenesis. These phases included injury, hematoma, angiogenesis,

and remodeling, and were identified based on image-based measurement of changes in total blood vessel length, average blood flow, and average SO_2 ($n = 6$). **b** Schematic illustrating the unique phases of angiogenic evolution during the calvarial defect healing cycle

For example, a slight decrease in total blood vessel length and intravascular SO_2 was observed during the injury phase, with $> 100\%$ increase in blood flow. The hematoma phase was characterized by an increase in all parameters (i.e., $\sim 100\%$ increase in total blood vessel length, 60% increase in blood flow, and a 20% increase in SO_2). During the angiogenesis phase, total blood vessel length continued to increase ($> 100\%$), SO_2 increased slightly ($< 10\%$), and blood flow returned to its level prior to the hematoma phase. Eventually, all the vascular parameters plateaued, which we defined as the remodeling phase, since it marked the end of angiogenic activities. These findings were consistent with observations of attenuated blood flow during the remodeling phase of bone healing reported by others [16, 17]. Finally, we successfully visualized the dynamics of angiogenic evolution in vivo via a time-lapse movie compiled from the structural and functional imaging data acquired over the entire 28 days of calvarial defect healing (Suppl. Video 2).

Discussion

Although the role of angiogenesis in bone healing is well established in terms of providing oxygen, nutrients, and cellular signals to generate a specialized bone healing microenvironment [18], the in vivo interplay between angiogenesis and osteogenesis has been underexplored due to the lack of appropriate tools. In this study, we used a multimodal imaging system in conjunction with multiscale image analyses and data visualizations to address these gaps. We leveraged the advantages of IOS, LSC, and μCT imaging along with a custom-designed image-processing pipeline, to characterize angiogenic evolution and osteogenesis over four weeks in a calvarial defect model. In spite of intra-animal variations, we observed that the robust structural changes in the angiogenic vasculature occurred during the first two weeks of defect healing. These data collectively indicated that the early stages of angiogenic evolution were characterized by concurrent changes in blood vessel length, volume, and density. Interestingly, during the 4th week of defect healing, although total blood vessel length and volume remained constant, there was an increase in blood vessel density. This could indicate that toward the end of the bone healing cycle, blood vessels tended to form a more interconnected and dense vascular network, with the increase in vessel density resulting from changes in vascular morphology instead of de novo vessel sprouting. Moreover, when we grouped blood vessels within the defect based on their tortuosity, segment length, and diameter, we observed that vessels with low tortuosity (< 1.2), short lengths ($< 100 \mu\text{m}$), and small to medium diameters ($< 30 \mu\text{m}$) exhibited the largest changes in density over four weeks. Prior studies have shown that calvarial angiogenesis involves vessels that stain strongly for

endothelial markers CD31 and Endomucin-1 (Emcn), i.e., “type H” vessels [19]. The morphological vascular data from this study are consistent with observations that these type H capillaries exhibit straight (i.e., less tortuous) columnar structure [20, 21].

The current gold-standard for quantifying bone growth in preclinical models is μCT [22]. In this study, we also demonstrated that in vivo 2D IOS imaging combined with semi-automated, machine-learning-based image segmentation yielded results comparable to those derived from volumetric μCT . Consequently, we could assess osteogenesis in vivo with IOS imaging and correlate it with angiogenic evolution over four weeks of defect healing.

While previous studies [23, 24] have assessed structural vascular changes during osteogenesis, changes in the function of angiogenic vessels in vivo remains poorly characterized. To the best of our knowledge, this is the first study to measure in vivo changes in multiple functional parameters (e.g., blood flow, intravascular SO_2 , and vascular maturity) during angiogenesis over the calvarial defect healing cycle.

Blood flow has historically been known to be an important player in regulating bone homeostasis and promoting bone growth [25, 26]. Early clinical studies have shown that tibial fracture healing was improved by increased blood flow [27]. Recently, distinct perfusion patterns were found in $\text{CD31}^{\text{high}}\text{Emcn}^{\text{high}}$ type-H vessels, which are key regulators in bone healing [7, 28]. However, blood flow modulation during bone healing is a complex process that involves a balance of proangiogenic and antiangiogenic factors [19], and remains poorly characterized in vivo. Therefore, we employed LSC imaging to characterize in vivo blood flow changes during angiogenic evolution over four weeks of defect healing. Since LSC exploits the movement of erythrocytes to assess in vivo perfusion, it does not require the administration of any extrinsic contrast or dye, and provides “microvascular-scale” perfusion data [9]. The major advantage of LSC is that it is minimally invasive and thus ideal for longitudinal in vivo imaging. Continuous LSC imaging revealed distinct patterns in perfusion during the different phases of bone healing. We postulate that the low blood flow at the beginning of injury were due to the rupture of blood vessels when creating the defect, and the increase in blood flow observed during the hematoma phase was a consequence of the inflammatory response. The decreased blood flow during angiogenesis was a result of the inflammation resolving and the presence of developing vessels within the defect regions. Collectively, our longitudinal in vivo data provided novel insights into blood flow modulation during bone healing.

The delivery of oxygen is one of the primary roles of angiogenic evolution during osteogenesis, because it is necessary for the multiple biological processes that ensure successful bone healing. These processes include aerobic

cell metabolism, enzyme activity, collagen synthesis, and the regulation of several angiogenic genes [29]. Although widely studied *in vitro* [30], the *in vivo* effects of oxygen on the cells involved in bone healing have been underexplored. Recently, we developed a method for mapping intravascular oxygen saturation (SO_2) *in vivo* that combined multi-wavelength IOS imaging with a vascular-centric estimation of optical path lengths [13]. Using this new method, we successfully characterized *in vivo* changes in intravascular SO_2 over the calvarial bone healing cycle. Interestingly, SO_2 was significantly higher in the angiogenic vessels around the leading edge of the defect during the period of most robust angiogenesis and perfusion (D10–12). This indicated that angiogenic vessels with elevated blood flow were also well-oxygenated to support bone growth. Toward the end of healing, angiogenic blood vessels had anastomosed to form a well-perfused vascular network that encompassed the field of view, with the SO_2 returning to normal levels. These observations were consistent with previous *in vivo* measurements made using two-photon microscopy and oxygen probes, demonstrating that the oxygen tension (pO_2) was elevated near the edge of the calvarial defect in the early stages of bone healing [31]. To the best of our knowledge, this is the first time that dynamic SO_2 changes have been continuously mapped *in vivo* at microvascular spatial scales, over the four week bone healing cascade. Such data could not only be used to characterize angiogenic evolution *in vivo*, but also phenotype the osteogenic niche in a wide array of preclinical models of bone healing. In addition, our multi-contrast *in vivo* imaging approach enabled further investigation into the role of oxygen in bone healing. For example, several studies have demonstrated the effectiveness of oxygen-generating scaffolds in supporting bone growth [32–34], and recent studies have begun to explore new pathways via which improved oxygenation can enhance osteogenesis [35].

It is noteworthy, that the existence of a dense vascular network does not necessarily result in better bone healing. Previous studies have shown that a dense, but poorly perfused capillary bed results in poor healing compared to a rapidly maturing vascular network [36]. Therefore, it was essential to evaluate the maturity of angiogenic vessels *in vivo* to determine if their functional impact on bone growth during the bone healing cascade. To map the relative maturity of the vasculature *in vivo*, we performed a carbogen gas challenge to induce smooth-muscle-mediated vasodilation of the blood vessels within the calvarial defect [37]. When a blood vessel dilates during carbogen gas inhalation, the resulting increase in blood flow can be measured *in vivo* by LSC imaging and the relative maturity of the vessels within the vascular network mapped in terms of the change in blood flow (ΔBF) relative to the baseline. Since immature angiogenic vessels are characterized by poor smooth muscle coverage, they are incapable of responding well to the carbogen gas challenge,

and therefore exhibited smaller changes in blood flow. Even at D0, in the absence of angiogenesis, we observed heterogeneous changes in blood flow (i.e., vascular maturity) within the defect. This might be attributable to the presence of blood vessels at different stages in their angiogenic cascade, or changes in blood flow upstream of the calvarial defect. Although previous studies have employed carbogen gas challenges as a functional indicator of vessel maturation [38], it is important to note that the criteria for defining vascular maturity can vary depending on the context or tissue type. To the best of our knowledge, within the context of the calvarial defect healing microenvironment, there have been no prior reports of the use of carbogen to distinguish mature from developing vessels. This made it challenging to distinguish these vascular phenotypes on the basis of an arbitrarily selected blood flow threshold from another study. To circumvent this issue, we employed K-means, a popular clustering technique, to classify vascular phenotypes based on similarities in their measured attributes [39]. Although K-means clustering can reveal meaningful patterns within the data [40], we acknowledge the importance of validating the results to ensure their biological significance. We did this by examining the average blood flow and radii of blood vessels in the two clusters (Suppl. Figure 1) and found that each vascular phenotype (i.e., mature vs. developing) was characterized by distinct perfusion and radii during the stages of angiogenic evolution.

From the longitudinal multicontrast images we acquired, we created time-lapse visualizations of angiogenic evolution *in vivo* during osteogenesis. Visualization of these real-time vascular changes revealed that new angiogenic vessels grew from the periosteum at the defect edges and anastomosed with dural vessels. This could be indicative of the cerebrovasculature potentially contributing to calvarial bone healing. While recent studies have addressed the cross-talk between brain and cranial bone [41], the role of the brain's vasculature in cranial bone growth remains unexplored. Finally, we successfully combined the *in vivo* imaging-derived structural and functional parameters to identify angiogenic evolution during the unique phases of calvarial bone healing. Previous studies have clearly defined the phases of healing in long bone fractures [42, 43], but angiogenic evolution has not been correlated with the phases of the calvarial bone healing cycle. Elucidating this spatio-temporal correlation could potentially help us design better clinical interventions and tissue-engineered constructs that enhance calvarial bone healing in patients. Using prior definitions of the bone healing phases [42, 43] and combining them with the structural and functional angiogenic changes we measured *in vivo*, we correlated the dynamics of angiogenic evolution with four phases of calvarial bone growth: injury, hematoma, angiogenesis, and remodeling. We believe that this provides us with a new rubric for characterizing

angiogenic evolution within the context of osteogenesis in addition to the conventional histological [44] or radiographic [45] methods.

Our results are consistent with those from other studies that have used complementary imaging modalities to investigate calvarial bone healing *in vivo*. For example, Holstein et al. [23] investigated healing of a subcritical-sized calvarial defect in a rodent model using intravital fluorescence microscopy. They too observed a robust increase in vascular density and blood vessel diameter during the first two weeks of healing, which plateaued toward the next two weeks of healing. Unlike the endogenous contrast employed in our study, Holstein et al. used intravascular injection of fluorescent tracers, and did not assess functional (e.g., blood flow) changes during angiogenesis. In addition, Huang et al. [24] investigated the spatiotemporal correlation between *in vivo* angiogenesis and osteogenesis with multiphoton microscopy (MPM). They exploited the superior resolution and tissue penetration of MPM to elegantly show that osteoblast activity was tightly coupled with angiogenesis near the leading edge of bone growth during the early stages of bone defect healing. The employed quantum dots to generate exogenous contrast, but did not assess *in vivo* perfusion changes. In addition to these optical methods, hybrid methods like photoacoustic imaging (PAI) have also been utilized to investigate healing during union and non-union bone formation in the long bone, and found that non-union bone exhibited lower SO_2 throughout the healing cascade [46]. PAI has also been used in conjunction with chronic cranial window models to study the murine brain vasculature [47], making it a promising method for investigating calvarial bone healing *in vivo*. Since PAI utilizes an acoustic signal that scatters less than the optical signal, it has great tissue penetration and an excellent ability to detect perfusion and oxygen saturation *in vivo* [48]. However, PAI is unable to generate endogenous contrast like the IOS contrast employed in our study, to assess bone growth *in vivo*. Therefore to characterize both, the structural and functional changes in a longitudinal *in vivo* study of bone and vascular remodeling, we employed a multimodality imaging system. A more detailed comparison of methods for imaging the vascular microenvironment in craniofacial bone tissue engineering applications can be found in [1].

Despite its advantages, our imaging pipeline does have certain limitations. First, since IOS and LSC are both 2D imaging techniques, we could not acquire depth-resolved *in vivo* angiogenesis and osteogenesis data. This may induce inaccuracies in quantifications of angiogenesis and osteogenesis because we are essentially acquiring 2D projections of 3D phenomena. One could envision addressing this by using depth-resolved imaging methods such as multi-photon microscopy [7], light-sheet microscopy [49] or μ CT to acquire the high-resolution, 3D vasculature and bone data for

comparison with *in vivo* 2D IOS data. Although we obviated this concern by validating our *in vivo* 2D osteogenesis measurements with 3D measurements from μ CT, doing the same for the vasculature data was beyond the scope of the current study paradigm. It is also possible for the complex and dynamically changing defect microenvironment to adversely affect *in vivo* imaging. For example, we observed a decrease in blood flow as measured by LSC imaging toward the end of the four week defect healing cycle. While the blood flow is known to revert to baseline levels toward the end of defect healing [26], the attenuated LSC signal may also be due to ingrowing bone. Since we derived maps of vessel maturity from blood flow responses to the carbogen challenge, extensive bone growth could also affect these measurements. In addition, since the carbogen challenge induced a systemic vasodilation, blood vessels with little or no smooth muscle coverage could exhibit increased blood flow due to vasodilation of blood vessels upstream of the calvarial defect. Finally, while multi-spectral IOS imaging provided us with intravascular SO_2 at microvascular resolution, this method cannot assess extravascular or tissue oxygenation within the defect.

In spite of these limitations, we are exploring the utility of such multimodality imaging workflows to evaluate the effects of novel tissue-engineered scaffolds on critical-sized calvarial bone healing. The real-time characterization of angiogenic evolution and osteogenesis *in vivo* could help evaluate the efficacy of such scaffolds, and iteratively improve scaffold design to expedite clinical translation [1].

Conclusion

In this work, we characterized angiogenic evolution during osteogenesis *in vivo* using a quantitative multimodality imaging approach. With this method, we successfully assessed structural and functional changes in bone and vascular morphology, perfusion, intravascular oxygenation, and blood vessel maturity over four weeks of bone healing in a preclinical calvarial defect model. We successfully correlated the dynamics of angiogenic evolution to the distinct phases of calvarial bone healing *in vivo*. In addition to glean new insights into bone healing biology, this technique could be harnessed to optimize the design and implementation of novel tissue engineering approaches. We believe these efforts could eventually usher in an era of “image-based tissue engineering.”

Supplementary Information The online version contains supplementary material available at <https://doi.org/10.1007/s10456-023-09899-0>.

Acknowledgments This work was supported by NIH/NCI grant nos. 2R01CA196701-06A1, 5R01CA237597-04 and 5R01DE027957-05.

Author contributions "YR, WG and APP designed the experiments. YR and APP wrote the main manuscript text and prepared figures. XC, JS, AB, WG assisted with imaging, data/image analyses and sample processing. All authors reviewed the manuscript."

Declarations

Competing interests The authors declare no competing interests.

References

- Ren Y, Senarathna J, Grayson WL, Pathak AP (2022) State-of-the-art techniques for imaging the vascular microenvironment in craniofacial bone tissue engineering applications. *Am J Physiol Cell Physiol* 323(5):C1524–C1538. <https://doi.org/10.1152/ajpcell.00195.2022>
- Grosso A, Burger MG, Lunger A, Schaefer DJ, Banfi A, Di Maggio N (2017) It takes two to tango: coupling of angiogenesis and osteogenesis for bone regeneration. *Front Bioeng Biotechnol* 5:68. <https://doi.org/10.3389/fbioe.2017.00068>
- Murphy MP, Quarto N, Longaker MT, Wan DC (2017) (*) Calvarial defects: cell-based reconstructive strategies in the murine model. *Tissue Eng Part C Methods* 23(12):971–981. <https://doi.org/10.1089/ten.TEC.2017.0230>
- Zuk PA (2008) Tissue engineering craniofacial defects with adult stem cells? Are we ready yet? *Pediatr Res* 63(5):478–486. <https://doi.org/10.1203/PDR.0b013e31816bdf36>
- Hankenson KD, Dishowitz M, Gray C, Schenker M (2011) Angiogenesis in bone regeneration. *Injury* 42(6):556–561. <https://doi.org/10.1016/j.injury.2011.03.035>
- Matusin DP, Fontes-Pereira AJ, Rosa P, Barboza T, de Souza SAL, von Kruger MA, Pereira WCA (2018) Exploring cortical bone density through the ultrasound integrated reflection coefficient. *Acta Orthop Bras* 26(4):255–259. <https://doi.org/10.1590/1413-785220182604177202>
- Zhai Y, Schilling K, Wang T, El Khatib M, Vinogradov S, Brown EB, Zhang X (2021) Spatiotemporal blood vessel specification at the osteogenesis and angiogenesis interface of biomimetic nanofiber-enabled bone tissue engineering. *Biomaterials* 276:121041. <https://doi.org/10.1016/j.biomaterials.2021.121041>
- Hillman EM (2007) Optical brain imaging in vivo: techniques and applications from animal to man. *J Biomed Opt* 12(5):051402. <https://doi.org/10.1117/1.2789693>
- Senarathna J, Rege A, Li N, Thakor NV (2013) Laser Speckle Contrast Imaging: theory, instrumentation and applications. *IEEE Rev Biomed Eng* 6:99–110. <https://doi.org/10.1109/RBME.2013.2243140>
- Bhargava A, Monteagudo B, Kushwaha P, Senarathna J, Ren Y, Riddle RC, Aggarwal M, Pathak AP (2022) VascuViz: a multimodality and multiscale imaging and visualization pipeline for vascular systems biology. *Nat Methods* 19(2):242–254. <https://doi.org/10.1038/s41592-021-01363-5>
- Schindelin J, Arganda-Carreras I, Frise E, Kaynig V, Longair M, Pietzsch T, Preibisch S, Rueden C, Saalfeld S, Schmid B, Tinevez JY, White DJ, Hartenstein V, Eliceiri K, Tomancak P, Cardona A (2012) Fiji: an open-source platform for biological-image analysis. *Nat Methods* 9(7):676–682. <https://doi.org/10.1038/nmeth.2019>
- Thevenaz P, Ruttimann UE, Unser M (1998) A pyramid approach to subpixel registration based on intensity. *IEEE Trans Image Process* 7(1):27–41. <https://doi.org/10.1109/83.650848>
- Ren Y, Senarathna J, Chu X, Grayson WL, Pathak AP (2022) Vascular-centric mapping of in vivo blood oxygen saturation in preclinical models. SSRN. <https://doi.org/10.2139/ssrn.4251020>
- Mendez A, Rindone AN, Batra N, Abbasnia P, Senarathna J, Gil S, Hadjiabadi D, Grayson WL, Pathak AP (2018) Phenotyping the microvasculature in critical-sized calvarial defects via multimodal optical imaging. *Tissue Eng Part C Methods* 24(7):430–440. <https://doi.org/10.1089/ten.TEC.2018.0090>
- Berg S, Kutra D, Kroeger T, Straehle CN, Kausler BX, Haubold C, Schiegg M, Ales J, Beier T, Rudy M, Eren K, Cervantes JI, Xu B, Beuttenmueller F, Wolny A, Zhang C, Koethe U, Hamprecht FA, Kreshuk A (2019) ilastik: interactive machine learning for (bio)image analysis. *Nat Methods* 16(12):1226–1232. <https://doi.org/10.1038/s41592-019-0582-9>
- Claes L, Recknagel S, Ignatius A (2012) Fracture healing under healthy and inflammatory conditions. *Nat Rev Rheumatol* 8(3):133–143. <https://doi.org/10.1038/nrrheum.2012.1>
- Claes L, Maurer-Klein N, Henke T, Gerngross H, Melnyk M, Augat P (2006) Moderate soft tissue trauma delays new bone formation only in the early phase of fracture healing. *J Orthop Res* 24(6):1178–1185. <https://doi.org/10.1002/jor.20173>
- Schipani E, Maes C, Carmeliet G, Semenza GL (2009) Regulation of osteogenesis-angiogenesis coupling by HIFs and VEGF. *J Bone Miner Res* 24(8):1347–1353. <https://doi.org/10.1359/jbmr.090602>
- Hendriks M, Ramasamy SK (2020) Blood vessels and vascular niches in bone development and physiological remodeling. *Front Cell Dev Biol* 8:602278. <https://doi.org/10.3389/fcell.2020.602278>
- Peng Y, Wu S, Li Y, Crane JL (2020) Type H blood vessels in bone modeling and remodeling. *Theranostics* 10(1):426–436. <https://doi.org/10.7150/thno.34126>
- Kusumbe AP, Ramasamy SK, Adams RH (2014) Coupling of angiogenesis and osteogenesis by a specific vessel subtype in bone. *Nature* 507(7492):323–328. <https://doi.org/10.1038/nature13145>
- Bouxsein ML, Boyd SK, Christiansen BA, Guldberg RE, Jepsen KJ, Muller R (2010) Guidelines for assessment of bone microstructure in rodents using micro-computed tomography. *J Bone Miner Res* 25(7):1468–1486. <https://doi.org/10.1002/jbmr.141>
- Holstein JH, Becker SC, Fiedler M, Garcia P, Histing T, Klein M, Laschke MW, Corsten M, Pohlemann T, Menger MD (2011) Intravital microscopic studies of angiogenesis during bone defect healing in mice calvaria. *Injury* 42(8):765–771. <https://doi.org/10.1016/j.injury.2010.11.020>
- Huang C, Ness VP, Yang X, Chen H, Luo J, Brown EB, Zhang X (2015) Spatiotemporal analyses of osteogenesis and angiogenesis via intravital imaging in cranial bone defect repair. *J Bone Miner Res* 30(7):1217–1230. <https://doi.org/10.1002/jbmr.2460>
- Grundnes O, Reikeras O (1992) Blood flow and mechanical properties of healing bone. Femoral osteotomies studied in rats. *Acta Orthop Scand* 63(5):487–491. <https://doi.org/10.3109/17453679209154720>
- Tomlinson RE, Silva MJ (2013) Skeletal blood flow in bone repair and maintenance. *Bone Res* 1(4):311–322. <https://doi.org/10.4248/BR201304002>
- Trueta J (1974) Blood supply and the rate of healing of tibial fractures. *Clin Orthop Relat Res* 105:11–26
- Ramasamy SK, Kusumbe AP, Schiller M, Zeuschner D, Bixel MG, Milia C, Gamrekelashvili J, Limbourg A, Medvinsky A, Santoro MM, Limbourg FP, Adams RH (2016) Blood flow controls bone vascular function and osteogenesis. *Nat Commun* 7:13601. <https://doi.org/10.1038/ncomms13601>
- Lu C, Saless N, Wang X, Sinha A, Decker S, Kazakia G, Hou H, Williams B, Swartz HM, Hunt TK, Micalau T, Marcucio RS (2013) The role of oxygen during fracture healing. *Bone* 52(1):220–229. <https://doi.org/10.1016/j.bone.2012.09.037>
- Arnett TR, Gibbons DC, Utting JC, Orriss IR, Hoebertz A, Rosendaal M, Meghji S (2003) Hypoxia is a major stimulator of

- osteoclast formation and bone resorption. *J Cell Physiol* 196(1):2–8. <https://doi.org/10.1002/jcp.10321>
31. Schilling K, El Khatib M, Plunkett S, Xue J, Xia Y, Vinogradov SA, Brown E, Zhang X (2019) Electrospun fiber mesh for high-resolution measurements of oxygen tension in cranial bone defect repair. *ACS Appl Mater Interfaces* 11(37):33548–33558. <https://doi.org/10.1021/acsami.9b08341>
 32. Suvarnapathaki S, Wu X, Zhang T, Nguyen MA, Goulopoulos AA, Wu B, Camci-Unal G (2022) Oxygen generating scaffolds regenerate critical size bone defects. *Bioact Mater* 13:64–81. <https://doi.org/10.1016/j.bioactmat.2021.11.002>
 33. Touri M, Moztaizadeh F, Abu Osman NA, Dehghan MM, Brouki Milan P, Farzad-Mohajeri S, Mozafari M (2020) Oxygen-releasing scaffolds for accelerated bone regeneration. *ACS Biomater Sci Eng* 6(5):2985–2994. <https://doi.org/10.1021/acsbomaterials.9b01789>
 34. Farris AL, Rindone AN, Grayson WL (2016) Oxygen delivering biomaterials for tissue engineering. *J Mater Chem B* 4(20):3422–3432. <https://doi.org/10.1039/C5TB02635K>
 35. Sun H, Xu J, Wang Y, Shen S, Xu X, Zhang L, Jiang Q (2023) Bone microenvironment regulative hydrogels with ROS scavenging and prolonged oxygen-generating for enhancing bone repair. *Bioact Mater* 24:477–496. <https://doi.org/10.1016/j.bioactmat.2022.12.021>
 36. DiPietro LA (2016) Angiogenesis and wound repair: when enough is enough. *J Leukoc Biol* 100(5):979–984. <https://doi.org/10.1189/jlb.4MR0316-102R>
 37. Ashkanian M, Gjedde A, Mouridsen K, Vafae M, Hansen KV, Ostergaard L, Andersen G (2009) Carbogen inhalation increases oxygen transport to hypoperfused brain tissue in patients with occlusive carotid artery disease: increased oxygen transport to hypoperfused brain. *Brain Res* 1304:90–95. <https://doi.org/10.1016/j.brainres.2009.09.076>
 38. Baudelet C, Cron GO, Gallez B (2006) Determination of the maturity and functionality of tumor vasculature by MRI: correlation between BOLD-MRI and DCE-MRI using P792 in experimental fibrosarcoma tumors. *Magn Reson Med* 56(5):1041–1049. <https://doi.org/10.1002/mrm.21047>
 39. Kim E, Zhang J, Hong K, Benoit NE, Pathak AP (2011) Vascular phenotyping of brain tumors using magnetic resonance microscopy (muMRI). *J Cereb Blood Flow Metab* 31(7):1623–1636. <https://doi.org/10.1038/jcbfm.2011.17>
 40. Oyelade J, Isewon I, Oladipupo F, Aromolaran O, Uwoghien E, Ameh F, Achas M, Adebisi E (2016) Clustering algorithms: their application to gene expression data. *Bioinform Biol Insights* 10:237–253. <https://doi.org/10.4137/BBI.S38316>
 41. Otto E, Knapstein PR, Jahn D, Appelt J, Frosch KH, Tsitsilonis S, Keller J (2020) Crosstalk of brain and bone-clinical observations and their molecular bases. *Int J Mol Sci*. <https://doi.org/10.3390/ijms21144946>
 42. Pfeiffenberger M, Damerou A, Lang A, Buttgerit F, Hoff P, Gaber T (2021) Fracture healing research-shift towards in vitro modeling? *Biomedicines*. <https://doi.org/10.3390/biomedicines9070748>
 43. Van der Ende J, Van Baardewijk LJ, Sier CF, Schipper IB (2013) Bone healing and mannose-binding lectin. *Int J Surg* 11(4):296–300. <https://doi.org/10.1016/j.ijsu.2013.02.022>
 44. Han Z, Bhavsar M, Leppik L, Oliveira KMC, Barker JH (2018) Histological scoring method to assess bone healing in critical size bone defect models. *Tissue Eng Part C Methods* 24(5):272–279. <https://doi.org/10.1089/ten.TEC.2017.0497>
 45. Zhang L, Zhang L, Lan X, Xu M, Mao Z, Lv H, Yao Q, Tang P (2014) Improvement in angiogenesis and osteogenesis with modified cannulated screws combined with VEGF/PLGA/fibrin glue in femoral neck fractures. *J Mater Sci Mater Med* 25(4):1165–1172. <https://doi.org/10.1007/s10856-013-5138-4>
 46. Menger MM, Korbel C, Bauer D, Bleimehl M, Tobias AL, Braun BJ, Herath SC, Rollmann MF, Laschke MW, Menger MD, Histing T (2022) Photoacoustic imaging for the study of oxygen saturation and total hemoglobin in bone healing and non-union formation. *Photoacoustics* 28:100409. <https://doi.org/10.1016/j.pacs.2022.100409>
 47. Wang Y, Xi L (2021) Chronic cranial window for photoacoustic imaging: a mini review. *Vis Comput Ind Biomed Art* 4(1):15. <https://doi.org/10.1186/s42492-021-00081-1>
 48. Steinberg I, Huland DM, Vermesh O, Frostig HE, Tummers WS, Gambhir SS (2019) Photoacoustic clinical imaging. *Photoacoustics* 14:77–98. <https://doi.org/10.1016/j.pacs.2019.05.001>
 49. Rindone AN, Liu X, Farhat S, Perdomo-Pantoja A, Witham TF, Coutu DL, Wan M, Grayson WL (2021) Quantitative 3D imaging of the cranial microvascular environment at single-cell resolution. *Nat Commun* 12(1):6219. <https://doi.org/10.1038/s41467-021-26455-w>

Publisher's Note Springer Nature remains neutral with regard to jurisdictional claims in published maps and institutional affiliations.

Springer Nature or its licensor (e.g. a society or other partner) holds exclusive rights to this article under a publishing agreement with the author(s) or other rightsholder(s); author self-archiving of the accepted manuscript version of this article is solely governed by the terms of such publishing agreement and applicable law.